SimHS-AFMfit-MD: An Integrative Approach to Deciphering Alpha-Actinin Atomic Conformational Dynamics

Kien Xuan Ngo[1,2,5,*], Takashi Sumikama[1, 5,], Rémi Vuillemot[3,5,*], Han Gia Nguyen[1], Ngan Thi Phuong Le[4], Sergei Grudinin[3,5,*]

[1]Nano Life Science Institute (WPI-NanoLSI), Kanazawa University, Kakuma-machi, Kanazawa 920-1192, Japan.

[2]Institute or Interdisciplinary Research in Science and Education (IFIRSE), ICISE, Quy Nhon, Vietnam.

[3]Univ. Grenoble Alpes, CNRS, Grenoble INP, LJK, 38000 Grenoble, France.

[4]Center for Bioscience and Biotechnology, University of Science, Vietnam National University, Ho Chi Minh City, Vietnam

[5]These authors contributed equally.

*Corresponding author: Kien Xuan Ngo, Takashi Sumikama, Rémi Vuillemot, Sergei Grudinin

Email:

ngoxuankien@staff.kanazawa-u.ac.jp (K.X.N.)

sumi@staff.kanazawa-u.ac.jp (T.S.)

remi.vuillemot@univ-grenoble-alpes.fr (R.V.)

sergei.grudinin@univ-grenoble-alpes.fr (S.G.)

Abstract

Many molecular systems, such as intrinsically disordered proteins and flexible multi-domain complexes, are highly dynamic and often inaccessible to conventional X-ray crystallography or cryo-EM due to their conformational heterogeneity and flexibility. As a result, resolving their atomic-level dynamics remains a significant challenge. In this study, we present SimHS-AFMfit-MD, an integrative framework that combines high-speed atomic force microscopy (HS-AFM), molecular dynamics (MD) simulations, and AFMfit-based structural modeling to reconstruct dynamic protein conformations at atomic resolution. Using alpha-actinin, an actin crosslinking protein, as a challenging test system, we show that AFMfit guided by nonlinear normal mode analysis (AFMfit-NMA) enables accurate structural fitting, while guiding AFMfit with MD trajectories (AFMfit-MD) further enhances the flexible fitting performance, achieving closer agreement with unbiased all-atom MD simulation results. This strategy allows us to convert thousands of three-dimensional HS-AFM images into atomic-scale conformational ensembles, revealing the twisting and bending transitions underlying Ca^{2+}-bound and Ca^{2+}-unbound alpha-actinin. Together, our results establish a hybrid computational–experimental approach that bridges the spatial and, to some extent, temporal resolution gaps between simulation and imaging, paving the way for real-time visualization of protein conformational dynamics at the atomic scale.

Keywords:

Alpha-actinin, HS-AFM, AFMfit-NMA, AFMfit-MD, MD Simulations, SimHS-AFMfit-MD, PCA.

Introduction

High-speed atomic force microscopy (HS-AFM) enables the imaging of biological structures and dynamics with nanometer-scale spatial resolution and millisecond temporal resolution. Generally, HS-AFM images capture three-dimensional (3D) surface data, incorporating two-dimensional (2D) lateral (x-y) and one-dimensional (1D) height (z) information encoded in pixel intensity[1]. This technique excels in imaging the

conformational states, dynamics, and functional properties of both single and complex protein molecules, as well as intricate biomolecular conformations, offering capabilities beyond those of other imaging methods such as cryo-electron microscopy and X-ray crystallography, which primarily yield static structural data.

The primary challenge in studying protein dynamics at atomic resolutions in real time using atomic force microscopy (AFM) lies in bridging gaps at the temporal and spatial scales. While HS-AFM can capture the dynamics of the three-dimensional (3D) surface structures of proteins with optimal performance in just a few tens of milliseconds (~20-100 ms/frame) and at nanometer scales (1 nm in the x–y plane; ~0.1 nm in the z–direction)[1–11], conventional molecular dynamics (MD) simulations typically explore atomic structures over much shorter time scales, from femtoseconds to microseconds[12–14]. Protein dynamics span a wide range of temporal scales (fs-µs), reflecting movements from atomic vibrations to molecular tumbling and larger collective motions that can be observed with nuclear magnetic resonance (NMR)[15,16] and MD simulations[13,17–21]. However, HS-AFM is particularly valuable for investigating slower processes, such as protein folding and conformational changes induced by drugs or protein interactions, which occur over temporal scales ranging from milliseconds to seconds. Traditional MD simulations face challenges in modeling large and complex biological systems because of computational constraints. However, recent advancements have substantially extended their capabilities, allowing the simulation of larger biomolecular systems over longer timescales[22–25]. One of the alternatives to MD is the Normal Mode analysis (NMA), another classical technique, which is well-suited to study near-equilibrium protein dynamics. NMA represents protein motions in terms of independent components and can capture them on fs to µs temporal resolution. Importantly, modern NMA engines are ultra-fast, much faster than MD, and scale linearly with the system size[26]. HS-AFM complements these advancements by enabling high-speed imaging of complex protein surface structures and dynamics and provides detailed insights into their functional activities[1]. NMR can simultaneously resolve the atomic structures and interactional dynamics but remains limited by the protein size, even with recent advancements in in-cell NMR.

The very recent AFMfit-NMA method reconstructs 3D atomic-resolution structures by an iterative fitting process that progressively adapts an input model (e.g., that obtained from a protein data bank (PDB), an AlphaFold prediction, or a model from MD simulations) to match the 3D molecular surface images captured from multiple experimental AFM observations. AFMfit-NMA mutually explores the rigid and flexible degrees of freedom via the fast Fourier transform (FFT) and the nonlinear rigid block normal-mode analysis (NOLB-NMA) methods, respectively[26–28]. Overcoming the discrepancies in temporal and spatial resolution between the experimental AFM data and simulations would enable a thorough comparison of different experimental and computational techniques in dynamic atomic structural biology. To render such an analysis, we have chosen alpha-actinin, a very challenging molecular system that experiences large-scale motions both in temporal and spatial domains.

Alpha-actinin is a key protein in the organization of the actin cytoskeleton and is crucial for maintaining the mechanical properties of cells. In humans, alpha-actinin isoforms 2 and 3, which are believed to be Ca^{2+} insensitive, are integral to the function of striated muscle and are regulated by phosphoinositides[29–34]. In contrast, non-muscle alpha-actinin isoforms 1 and 4 are Ca^{2+}-sensitive[35–37]. Previous studies have elucidated the atomic structure of these muscle and non-muscle alpha-actinin isoforms via techniques such as X-ray scattering[35–37]. However, these methods often fail to capture the dynamic conformational changes of these molecules. An understanding of these changes is crucial for elucidating the role of alpha-actinin in actin filament crosslinking and the associated structural changes under unipolar and bipolar crosslinking states.

In this study, we aimed to explore the atomic conformational dynamics of alpha-actinin through a multidimensional approach. To do so, we developed a novel workflow, SimHS-AFMfit-MD, that transforms the three-dimensional (3D) surface AFM images into 3D atomic conformations by integrating HS-AFM with the normal mode-based flexible fitting algorithm AFMfit-NMA[38] and MD simulations[13,17–21]. This strategy bridges the spatial and, to some extent, temporal gaps between the experimental AFM data and MD/NMA simulations. Our pipeline enables the interpretation of the HS-AFM data with the 3D atomic models and overcomes the limitations of direct visualization techniques. MD

simulations, together with the NMA, have extended our understanding of protein dynamics by capturing atomic structural transitions on the microsecond timescale, providing complementary insights into molecular flexibility and stability[39].

Results

Overview of the methodology for integrating HS-AFM with AFMfit and MD simulations

The focus of this study was to develop an innovative workflow to analyze and understand how proteins change their atomic structure and how these conformational changes are related to their functions. Equally crucial, however, is understanding the protein dynamics, such as folding and interaction processes, since these processes directly influence the biological roles of proteins. HS-AFM can provide insights into the dynamic structural changes in proteins during their functional processes in solution[1,40,41]. While having high temporal resolution, HS-AFM lacks the atomic spatial resolution of other experimental techniques, such as X-ray crystallography or cryo-electron microscopy (cryo-EM). Therefore, one of the principal challenges with AFM lies in interpreting its low-resolution, 3D surface images into detailed 3D atomic conformations.

The innovative aspect of our approach lies in the combination of several techniques: HS-AFM, AFMfit (a method for fitting AFM images), nonlinear NMA, and MD simulations to establish the SimHS-AFMfit-MD pipeline (**Fig. 1**). This workflow consists of four key steps: (i) acquisition of experimental AFM images and protein models (PDB files); (ii-iii) AFM fitting (i.e. AFMfit-NMA, AFMfit-MD) and MD simulations to generate libraries of atomic conformations (PDB); and (iv) PCA analysis to classify the dynamic atomic conformations based on their principal components (PCs) (**Fig. 1C**). By integrating these techniques, we can obtain a more comprehensive view of the 3D atomic structure of proteins, along with their dynamics and conformational changes during functional activities.

We used our methodology to analyze the conformational changes in the Ca^{2+}-bound and Ca^{2+}-unbound alpha-actinin over milliseconds to seconds and to determine the atomic conformational dynamics of this protein. Alpha-actinin is an antiparallel homodimer with

150 a molecular weight exceeding 200 kDa. The structure of chicken gizzard smooth muscle
151 alpha-actinin (PDB: 1SJJ)[34] consists of the following domains: an N-terminal actin binding
152 domain (ABD), in which the two calponin homology 1 and 2 (CH1, CH2) domains are in
153 extensive contact; a central region containing four spectrin-like repeat (SR1-SR4) or rod
154 domains; and a C-terminal calmodulin-like domain (CaMD) that includes two pairs of EF-
155 hand motifs (EF12 and EF34), and the EF12 domain is responsible for Ca^{2+} binding. The
156 two ABDs undergo a 90-degree rotation, enabling alpha-actinin to crosslink the actin
157 filaments in nearly any orientation[34] (**Fig. 1A, B**).
158 We applied SimHS-AFMfit-MD to generate libraries of atomic models in different
159 conformations for both Ca^{2+}-bound and Ca^{2+}-unbound alpha-actinin using a workflow
160 shown in **Fig. 1C**. This provided insights into their atomistic structures and collective
161 motions over time. First, we gently immobilized alpha-actinin molecules on mica and HS-
162 AFM collected data with a typical imaging rate of 100 ms per frame (**Supplementary**
163 **Video 1**). We then processed the HS-AFM with AFMfit-NMA or AFMfit-MD, starting
164 with a reference atomic model derived from the MD simulations (**Supplementary Videos**
165 **2-3**). Specifically, AFMfit-NMA fits this reference model to the experimental AFM data
166 by generating pseudo-AFM images derived from this reference model over two fitting steps.
167 The first step was rigid fitting, where the reference model was rigidly aligned with the
168 AFM experimental data to obtain an optimal pose using an exhaustive search algorithm
169 based on the FFT. In the second flexible fitting step, the aligned models were flexibly
170 deformed using the NOLB technique[26] to obtain the optimal elastic alignment of the atomic
171 models to multiple AFM observations. By applying this iterative process to our alpha-
172 actinin AFM data, we collected the corresponding conformational libraries for the protein
173 (see the Supplementary Methods). Simultaneously, the same initial protein model (PDB:
174 1SJJ)[34] was used as the starting point for the MD simulations (see the Supplementary
175 Methods). The simulations were conducted over a timescale of 1 microsecond, resulting in
176 a set of conformation libraries for alpha-actinin. We then analyzed the atomic
177 conformations obtained from AFMfit-NMA, AFMfit-MD, and MD simulations using
178 principal component analysis (PCA). This analysis allowed us to interpret the

conformational ensembles as representing the dynamic behavior of the atomistic structure of the proteins.

Ca^{2+} binding affects smooth muscle alpha-actinin flexibility

First, we employed state-of-the-art HS-AFM to obtain high spatiotemporal resolution images of alpha-actinin. Three-dimensional molecular surface images of the individual Ca^{2+}-bound and Ca^{2+}-unbound alpha-actinin on mica were continuously recorded under near-physiological conditions at an imaging rate of 100 ms per frame (**Fig. 2, Supplementary Table 1, Supplementary Video 1**). The conformational dynamics of thousands of alpha-actinin molecules, including bending and twisting motions, were successfully captured and visualized in our AFM images (red and yellow arrowheads, **Fig. 2A**). To distinguish the conformational dynamics between these two states, we semi-automatically tracked the positions (x, y, and z coordinates) of the two ABD spheres on opposite sides of multiple alpha-actinin molecules over sequential frames and calculated the distance between their peak heights. HS-AFM analysis demonstrated that while the ensemble lengths of alpha-actinin were similar in the presence and absence of Ca^{2+}, there was a significant difference in the ensemble heights between the two states. From the HS-AFM dataset, the mean ± SD heights and lengths were 5.7 ± 0.9 nm (N = 3040) and 25.1 ± 2.3 nm (N = 1941) for Ca^{2+}-bound alpha-actinin and 4.8 ± 0.7 nm (N = 6080) and 25.0 ± 3.2 nm (N = 3885) for Ca^{2+}-unbound alpha-actinin. The results revealed statistically significant differences ($p < 0.05$) in the height distributions, but no significant difference in length between the Ca^{2+}-bound and Ca^{2+}-unbound alpha-actinin (**Fig. 2B**).

Investigating alpha-actinin dynamics at the atomic level via SimHS-AFMfit-MD

Our HS-AFM–based analyses helped elucidate some of the characteristics of alpha-actinin, including its fluctuations in height and length over time. However, these conventional AFM processing techniques were unable to reveal critical insights into the conformational dynamics of alpha-actinin, such as its bending and twisting motions, as they only provided its surface structure (**Fig. 2A**). But an understanding of these motions is essential to grasp the mechanical influence of the actin-crosslinking function of alpha-actinin on the structure,

209 dynamics, and function of actin filaments. Thus, we developed the SimHS-AFMfit-MD
210 pipeline by integrating HS-AFM with AFMfit-NMA or AFMfit-MD, and MD simulations.
211 This pipeline includes four steps (**Fig. 1C**) and allows us to further investigate the dynamics
212 and atomic structure of alpha-actinin. We utilized AFMfit-NMA and AFMfit-MD to
213 transform the 3D molecular surfaces of alpha-actinin, obtained from HS-AFM, into 3D
214 atomic conformations (**Supplementary Fig. 1A, Supplementary Videos 2-3**). Through
215 this method, we created libraries of atomic conformations for the Ca^{2+}-bound and Ca^{2+}-
216 unbound alpha-actinin states (**Fig. 3A-C**). These conformations were then aligned to
217 compare the dynamics of the two states based on the AFMfit-NMA, AFMfit-MD, and the
218 MD simulations. The distribution of Cα positions was broader in the AFMfit-NMA
219 analysis compared to the MD simulations (**Figs. 3A vs 3C**), yet the distributions were quite
220 similar between AFMfit-MD and the MD simulations (**Figs. 3B vs 3C**). Notably,
221 integrating MD trajectory information into AFMfit (AFMfit-MD) resulted in a
222 conformational library that more closely aligned the one generated by MD simulations
223 (**Figs. 3B vs 3C**). NMA-based structural fits, captured less extensive molecular change
224 between Ca^{2+}-bound and Ca^{2+}-unbound states than the 1.0-microsecond unbiased MD
225 simulations and AFMfit-MD. Additionally, substrate interactions that might have occurred
226 during the AFM analysis, which were not present in the MD simulation results, could
227 somehow influence the dynamics of alpha-actinin sitting on mica, even though
228 immobilization conditions were optimized in our HS-AFM experiments.
229 The root mean square fluctuation (RMSF), which is a commonly used metric for evaluating
230 the flexibility and mobility of atoms or residues in proteins, was employed to quantify the
231 deviation of each Cα atom from its average position using the conformational libraries
232 generated with the AFMfit-NMA, AFMfit-MD, and MD simulations (**Fig. 3D**). The results
233 revealed the dynamic motions of CH1-CH2 within the ABD, neck, and EF12-EF34
234 domains. However, the rod (SR1-SR4) domains exhibited relatively high rigidity.
235 Although there was a difference in the estimated fluctuation magnitudes of alpha-actinin
236 between AFMfit-NMA and MD simulations, integrating MD trajectory guidance into
237 AFMfit (i.e. AFMfit-MD) produced results that more closely aligned with those obtained
238 from MD simulations. The SimHS-AFM-MD analysis consistently showed that Ca^{2+}

239 binding slightly reduced the motion of the CH1-CH2 and EF12-EF34 domains near the
240 neck in muscle alpha-actinin.
241
242 **Classifying the dynamic atomic conformations of alpha-actinin via PCA**
243 PCA is a statistical method used to reduce the dimensionality of a dataset while retaining
244 its most significant variations. It is highly effective in identifying and classifying the
245 collective motions of individual protein domains using principal components (PCs).
246 First, we determined the ensemble of the atomic motions of the Ca^{2+}-bound and Ca^{2+}-
247 unbound alpha-actinin by analyzing the libraries of the conformations obtained from the
248 AFMfit-NMA, AFMfit-MD, and MD simulations and projected these motions onto a
249 common PCA space (**Fig. 4A, Supplementary Videos 4-6**). The eigenvalues of principal
250 components 1 (PC1), PC2, and PC3 were used to determine the percentage contribution of
251 each motion. PC1 (27%) primarily captured the ensemble of the bending motions in the x-
252 axis, PC2 (17%) represented the bending motions in the y-axis, and PC3 (10%) described
253 the twisting motions.
254 To compare the data obtained from the AFMfit-NMA, AFMfit-MD, and MD simulations,
255 we projected the conformational libraries of the Ca^{2+}-bound and Ca^{2+}-unbound alpha-
256 actinin generated from the AFMfit-NMA, AFMfit-MD, and MD simulations onto a
257 common PCA space and plotted the distributions of PC1 versus PC2 and PC1 versus PC3
258 (**Fig. 4B**). For both the Ca^{2+}-bound and Ca^{2+}-unbound states, PC1 derived from the AFMfit-
259 NMA conformational libraries exhibited a broader distribution of ensemble bending
260 motions along the x-axis compared with those from the AFMfit-MD and MD simulation
261 libraries, which showed similarly narrower distributions.
262 Despite the differences in the fluctuation magnitudes exhibited by the AFMfit-NMA results
263 and MD simulations, the integration of MD trajectory guidance into AFMfit produced a
264 similar distribution of fluctuation (**Fig. 4B**), the PC2 value consistently captured the
265 ensemble bending motions in the y-axis of both the Ca^{2+}-bound and the Ca^{2+}-unbound
266 states. These results indicated the agreement between the three methods. We observed a
267 similar trend for PC3, which captured a comparable degree of twisting motions in the Ca^{2+}-
268 bound and Ca^{2+}-unbound states between AFMfit-MD and MD simulation methods.

However, PC3 exhibited distinct fluctuations when compared to results obtained from AFMfit-NMA. Thus, we can conclude that PCA successfully analyzed and categorized the physical motions in the Ca^{2+}-bound and Ca^{2+}-unbound alpha-actinin at atomistic scales using PC1, PC2, and PC3, derived from the conformations generated via AFMfit-NMA and AFMfit-MD, analysis and the MD simulations (**Fig. 4**).

Across all results, the eigenvector components or motions represented by the blue arrows in SR1 and SR4 were small in magnitude. However, those in SR2 and SR3 showed almost no motion (**Fig. 4A**). These results confirmed the rigidity of the rod domain. In contrast, prominent eigenvector components were observed in CH1–CH2 within the ABD, in EF12–EF34, and in the neck domain, indicating relatively high flexibility in these regions. In summary, our SimHS-AFMfit-MD approach demonstrates an outstanding ability to capture and categorize the atomic conformational dynamics of the Ca^{2+}-bound and Ca^{2+}-unbound alpha-actinin.

Quantitative analysis of domain distances in alpha-actinin

To more accurately characterize the dynamic atomic conformational changes in Ca^{2+}-bound and Ca^{2+}-unbound alpha-actinin, we conducted a quantitative analysis of the atomic-level movements of individual domains using AFMfit-NMA, AFMfit-MD, and MD simulations. We then compared the results across methods by focusing on the distances between the CH1, CH2, EF12, and EF34 domains within the ABD and CaMD (**Fig. 5, Supplementary Table 2**). This analysis allowed us to successfully capture the fluctuations between domains and assess the similarities and differences between the Ca^{2+}-bound and Ca^{2+}-unbound states.

The results from AFMfit-MD and MD simulations corroborated the molecular dynamics observed in the Ca^{2+}-bound and Ca^{2+}-unbound alpha-actinin structures obtained through AFMfit-NMA, revealing similar trends at the atomic level (**Fig. 5**). Notably, AFMfit-MD and MD simulations revealed greater magnitudes of domain fluctuations compared to AFMfit-NMA (**Figs. 5B vs 5CD**). The results from AFMfit-MD and MD simulations consistently showed that Ca^{2+} binding to the EF12 domain reduced fluctuations in alpha-actinin dynamics, whereas this effect captured via PC1 was not as clearly observed in the

AFMfit-NMA results. In conclusion, our SimHS-AFMfit-MD pipeline successfully captured and characterized the atomic conformations and dynamic behaviors of both Ca^{2+}-bound and Ca^{2+}-unbound alpha-actinin across nanosecond to millisecond timescales, thereby bridging the spatial and, to some extent, temporal resolution gaps between experimental and computational approaches. This approach addresses the limitations of earlier static atomic structural studies that relied solely on X-ray scattering[33,35–37] and cryo-EM[34].

Quantitative analysis of bending and twisting motions in alpha-actinin

To further capture the collective motions of the molecules and assess the physical impact of its actin crosslinking function, we analyzed the bending and twisting angles of the ABD relative to the rod domain in both the Ca^{2+}-bound and Ca^{2+}-unbound alpha-actinin using conformational libraries derived from AFMfit-NMA, AFMfit-MD, and MD simulations (**Fig. 6**). As described above, PCA of the conformations confirmed the rigidity of the rod domain (SR2-SR3). With reference to a vector defined along the Cα positions within the SR2-SR3 domain (**Fig. 6A**), the bending angles were measured relative to the center of mass of the Cα atoms in the CH1, CH2, EF12, and EF34 domains near the neck in chain 1 and chain 2. To measure the twisting angles, the vectors were defined by linking the centers of mass of the Cα atoms between the EF12-EF34 and CH1-CH2 domains, and the angles of these vectors were measured relative to the SR2-SR3-aligned reference vector (**Fig. 6B**). The distributions of bending and twisting angles in chain 1 and chain 2, with and without Ca^{2+} binding, were analyzed to more effectively capture the directions of the collective motions, whether in x-axis or y-axis direction. Quantitative measurements of the bending and twisting angles in chains 1 and 2 of the Ca^{2+}-bound and Ca^{2+}-unbound alpha-actinin based on the AFMfit-NMA and MD simulations (**Fig. 6, Supplementary Table 3**) confirmed the flexibility of the bending and twisting motions of alpha-actinin. Despite the previously identified differences between the methods in their ability to estimate the magnitudes of fluctuation, the AFMfit-NMA, AFMfit-MD, and the MD simulations showed that Ca^{2+} binding could restrict these motions to some extent. Our approach effectively refined and categorized the impact of Ca^{2+} on physical motions, such as the

329 bending and twisting of smooth muscle alpha-actinin. When the ensemble of
330 conformations obtained using our method was compared with those obtained from other
331 techniques, such as cryo-EM[6], which reported that non muscle alpha-actinin was not
332 sensitive to Ca^{2+}, our results not only aligned with these findings but also offered a more
333 detailed understanding of its dynamic behavior than cryo-EM.
334

335 **Discussion**

336 Time-resolved cryo-EM is emerging as a powerful tool for investigating protein dynamics
337 and atomic conformations simultaneously[42–44]. Its potential can be further enhanced by
338 integrating approaches such as cryo-EM flexible fitting[45] or computational methods.
339 Additionally, advanced NMR spectroscopy provides complementary insights and captures
340 both structural and dynamic aspects of proteins during interactions[15,16,46,47].
341 While NMR spectroscopy excels in studying protein structure, dynamics, and interactions,
342 it has limitations. Traditional solution-state NMR is most effective for proteins under ~30–
343 50 kDa, although techniques such as transverse relaxation-optimized spectroscopy
344 (TROSY) extend this range to ~100 kDa. Larger proteins suffer from the signal overlap
345 and line broadening because of the slow molecular tumbling and transverse relaxation.
346 Compared with cryo-EM and X-ray crystallography, NMR also has lower sensitivity, and
347 peak overlap complicates resonance assignments in complex systems[16,48–50].
348 In dynamic studies, NMR provides insights into timescales from picoseconds to seconds
349 but struggles with motions faster than 10 ps or slower than seconds to minutes[49,50]. Solid-
350 state NMR remains challenging for membrane proteins because of the need for extensive
351 isotopic labeling and specialized pulse sequences[50]. Additionally, weak or transient
352 interactions can produce signals that are too faint for accurate characterization. Sample
353 preparation and long data acquisition times (hours to days) further risk protein degradation
354 or aggregation[48].
355 While cryo-EM surpasses NMR in resolving large protein complexes (>100 kDa), it is less
356 effective for studying dynamics[51]. However, these techniques can complement each other[52].
357 Other single-molecule techniques, such as FRET, can complement NMR for fast

358 dynamics[53], but no standalone method can perfectly capture the atomic structures,
359 dynamics, and interactions simultaneously.
360 Despite the inherent limitations of AFM, such as its ability to capture only 3D surface
361 images of soft and biological samples with a maximum spatial resolution of ~1 nm in the
362 x–y plane and ~0.1 nm in the z dimension, recent advancements in HS-AFM have
363 significantly increased its temporal resolution[1]. Due to these improvements, imaging at
364 timescales of a few tens of milliseconds or faster can be performed and enable a more
365 precise characterization of protein dynamics. HS-AFM has the ability to image large
366 complex protein systems without the need for chemical labeling, enabling the simultaneous
367 capture of nanostructures, dynamics, and protein interactions or assemblies under near-
368 physiological conditions; this capability surpasses those of NMR, x-ray crystallography,
369 and cryo-EM. Additionally, by integrating HS-AFM with the AFMfit-NMA[38] and AFMfit-
370 MD and MD simulations through SimHS-AFMfit-MD, we generated comprehensive
371 libraries of atomic conformations, facilitating the investigation of the physical motions and
372 atomic structures of alpha-actinin through PCA and providing a robust framework for
373 improving the interpretation of low-resolution experimental AFM data. For instance, the
374 twisting and bending motions of alpha-actinin were cross-validated using AFMfit-based
375 NMA and AFMfit guided by MD trajectories and unbiased all-atom MD simulations,
376 confirming the robustness of the integrated SimHS-AFMfit-MD approach and offering
377 deeper insights into the physical dynamics and actin crosslinking function of alpha-actinin.
378 This capability potentially contributes to better understanding of previous static structural
379 studies using X-ray diffraction[54,55] and cryo-EM[56,57]. Ultimately, this integration addresses
380 the spatial and temporal limitations of experimental AFM and MD simulation data and
381 facilitates the study of the atomic conformational dynamics of complex protein assemblies.
382 Apparently, the data obtained through SimHS-AFMfit-MD can be useful for developing
383 force fields to simulate complex protein models, as demonstrated in previous studies[22–25].
384 Force fields are crucial for accurately validating the interatomic forces acting between the
385 atoms composing the system since they account for the intermolecular or interatomic
386 interactions and energy minimization[58,59]. More broadly, the conformational libraries could
387 also serve as training data for the deep learning models[60–62] to predict the pseudoatomic

structures across different timescales (i.e., prediction of protein dynamics) and help bridge the gap between the experimental and computational methods. In this context, recent advancements in three-dimensional localization AFM (3D-LAFM) have successfully transformed the AFM data into 3D density data[63], facilitating large-scale 3D atomic AFM data generation through the integration with the MD simulations.

Conclusion

SimHS-AFMfit-MD provides an innovative approach for overcoming the spatial and temporal resolution limitations of imaging and simulation data. This method can be further developed, such as by its integration with deep learning, NMR, cryo-EM, cryo-ET, or in silico AFM[64], to bridge the spatiotemporal resolution gaps between HS-AFM and the MD simulations and to capture and predict protein dynamics; this has enabled real-time studies of the atomic conformational dynamics of complex proteins and surpassing the capabilities of individual techniques. Our approach facilitates new possibilities for advancing the understanding of the atomic structural dynamics of complex protein assemblies that mimic cellular machines.

Methods

Proteins

Chicken gizzard smooth muscle alpha-actinin (isoform 2)[33] was obtained from Cytoskeletons (Sigma, Japan).

HS-AFM Analysis

We employed high-speed atomic force microscopy (HS-AFM), as previously described[7,8,40,65], to capture the dynamic conformations of alpha-actinin in various states, providing high-speed imaging and three-dimensional (3D) surface structure of the protein at nanometer resolution. Chicken gizzard smooth muscle alpha-actinin, an isoform 2 (Sigma, Japan), was diluted to 30 nM and imaged in F-buffer containing 20 mM KCl, 10 mM PIPES-KOH (pH 6.8), 0.5 mM $MgCl_2$, 0.25 mM EGTA, 0.25 mM DTT, and 0.5 mM ATP. To observe the dynamic conformational changes in alpha-actinin with $CaCl_2$, the

proteins were imaged in the same F-buffer with the addition of 0.1-0.2 mM $CaCl_2$. Length and height of alpha-actinin were semi-automatical analyzed using Kodec software with the source code[7].

AFMfit-NMA Analysis

The AFMfit-NMA protocol was originally developed to fit 3D atomic structures into 3D surface AFM images[38]. In this study, AFMfit-NMA started the fitting procedure with the initial models used in MD simulations. These models were derived from PDB entry 1SJJ[34] for both Ca^{2+}-bound and Ca^{2+}-unbound states, serving as a reference atomic model.

The AFMfit-NMA protocol began by cropping AFM images into sub-images, referred to as particles, that corresponded to the molecule of interest. This cropping operation was semi-automatic: an initial automated process identified potential particles using the particle-tracking toolkit TrackPy (Allan, D. B., Caswell, T., Keim, N. C., van der Wel, C. M., & Verweij, R. W. (2021). soft-matter/trackpy: Trackpy v0.5.0 (v0.5.0). Zenodo. https://doi.org/10.5281/zenodo.4682814), followed by a manual verification step to eliminate any false positives.

We processed the extracted particles using AFMfit-NMA, which estimated the optimal rigid and flexible degrees of freedom for the initial model. The alignment procedure maximized the similarity between the particles and the pseudo-AFM images calculated from the model. The calculation of these pseudo-AFM images had to be adjusted to match the experimental conditions. Specifically, we estimated the shape of the experimental probe tip to account accurately for the tip convolution effect. We conducted this estimation through an exhaustive search of a smoothness parameter across the entire set of particles.

AFMfit proceeded in two steps. In the first step, it performed a rigid-body pre-alignment of the model to the particles using a 5D exhaustive search accelerated by FFT. This process estimated the relative position (two translational degrees of freedom) and orientation (three rotational degrees of freedom) of each particle. The angular step for the rotational search was set to 10° and restricted to flat orientations of alpha-actinin to accelerate the computations. The translational step in the z-direction was set to 1 Å.

In the second step, AFMfit combined the continuous rigid and flexible alignments of the model to the particle using the non-linear normal mode analysis method NOLB[26]. NOLB calculated normal modes using the Rotation-Translation of Blocks (RTB) approximation on an Elastic Network Model (ENM). We set the interaction cutoff in the ENM to 8 Å. We restricted the possible motions of our model to the sixteen lowest frequency normal modes, among which ten modes were the flexible motions describing the most collective motions of alpha-actinin, including bending and twisting. The six normal modes left corresponded to rigid translations and rigid rotations in 3D. We used them to account for continuous rigid rearrangement that could be necessary when flexibly deformating the model. According to the AFMfit-NMA method, we iteratively calculated the optimal linear approximation of the normal mode displacement that fitted the particle. Then, we carried out a non-linear extrapolation of the motion following the NOLB methodology. We iterated over the linear approximation and non-linear extrapolation until convergence, which, in practice, was obtained in five iterations.

The flexible fitting procedure aimed to keep a balance between minimizing deformations from the initial model – thus preserving its structure and preventing unrealistic distortions – and maximizing similarity to the data. This balance was controlled by a hyperparameter λ. We estimated the optimal value of λ through an exhaustive search, conducting flexible fitting on a sample of particles. Our goal was to achieve a maximum average root-mean-square deviation (RMSD) of 10 Å from the initial model. We chose this threshold to reflect the typical range of motions observed in molecular dynamics (MD) simulations of alpha-actinin. Ultimately, we found that the optimal value for λ was 7.5 (**Supplementary Fig. 1**).

AFMfit-MD

The original AFMfit method (we refer to it here as AFMFit-NMA) employed NMA and the elastic network model to estimate the low-dimensional subspace of protein motions. In the current AFMfit-MD algorithm, we utilize presampled MD conformations for estimating this subspace instead of the NMA. Concretely, we do the following. Firstly, we structurally align all the MD frames on the reference one by minimizing the corresponding RMSD using the QCP library[66]. We use the first MD frame as a reference. Then, we

linearly project all the frames into the RTB six-dimensional SE(3) space, constructed at the reference conformation of the system. By default, we are using each residue as a rigid block. After, we build a $6B \times 6B$ covariance matrix in this space, similarly to the RTB-projected Hessian matrix in the RTB NMA approaches[66]. Eigenvectors of this matrix correspond to the instantaneous linear and angular velocities of each rigid block, protein's residue in our case. We shall mention that if the number of frames in a trajectory is much smaller than *6B*, it is computationally more advantageous to instead compute SVD vectors on the original matrix of RTB projected coordinates. Then, we proceed with the NOLB *nonlinear* extrapolation of the computed eigenmotions and the AFMfit fitting procedure.

AFMfit-MD theory

Let us consider a rigid body parameterized with a 3-vector of its centre of mass $\vec{c}$, a 3-vector of its orientation $\vec{\theta}$, its total mass m, and its *inertia tensor* I, computed relatively to the center of mass. Assuming that it is composed of k individual atoms at positions $\overrightarrow{x_k}$ with masses m_k, we can write two momentum conservation laws as

$$m\dot{\vec{c}} = \sum_k \quad m_k \dot{\overrightarrow{x_k}}$$

$$I\dot{\vec{\theta}} = \sum_k \quad m_k(\overrightarrow{x_k} - \vec{c}) \times \dot{\overrightarrow{x_k}}$$

These conservation laws provide a linear relationship between *instantaneous* motions in the Cartesian and the rigid-body spaces. We can compactly represent them with linear projector operators written in a matrix form. Indeed, having a molecular system composed of N atoms, we can split it into B rigid blocks, which can be B residues in the case of a protein. Then, a $6B \times 3N$ projector matrix P will provide a relationship between the two spaces. It is composed of B positional P^c and orientational P^θ sub-matrices of size $3 \times 3N_b$ each, where N_b is the number of atoms in the b-th rigid body. Each 3×3 element of these matrices reads as

$$P_k^c = \frac{m_k}{m} E$$

$$P_k^\theta = m_k I^{-1} [\overrightarrow{x_k} - \vec{c}]_\times$$

On the next step, we construct a $6B \times 6B$ covariance matrix C in the RTB space from a normalized $3N \times t$ matrix X collected from t MD frames,

$$C = \frac{1}{t-1} P(X - \bar{X})(X - \bar{X})^T P^T,$$

where matrix $\bar{X}$ corresponds to a mean molecular conformation over t frames. We decompose C as $C = V\Lambda V^T$, where V is a $6B \times 6B$ matrix with each column defining an RTB eigenvector or a principal component that we interpret as an instantaneous linear and angular velocity of each rigid block (residue). Λ is a diagonal matrix containing the eigenvalues, which may depend on the sampling biases along the MD trajectory. Finally, we follow the original AFMFit strategy. Each eigenvector V has six components per residue: three correspond to the instantaneous linear velocities $\vec{v}$ and the other three to the instantaneous angular velocities $\vec{\omega}$. We extrapolate the coordinate $\vec{x}$ of each atom in a residue at an amplitude α as

$$\vec{x}(\alpha) = R(\alpha||\vec{\omega}||_2, \overrightarrow{\omega/}||\vec{\omega}||_2)(\vec{x}(0) - \vec{r}) + \vec{r} + \alpha\vec{\omega}(\vec{v} \cdot \vec{\omega})/||\vec{\omega}||_2^2,$$

where we parameterize rigid rotation R with an angle-axis notation. Here, the center of rotation $\vec{r}$ for a residue with the center of mass $\vec{c}$ is given by

$$\vec{r} = \vec{c} + (\vec{\omega} \times \vec{v})/||\vec{\omega}||_2^2.$$

Following AFMFit, we also include into the calculations six zero-frequency eigenvectors corresponding to rigid-body translations and rotations. However, we compute them analytically. After this procedure, we follow the original flexible fitting step from AFMFit.

MD Simulations

Molecular dynamics (MD) simulations were performed to generate libraries of conformations for Ca^{2+}-bound and Ca^{2+}-unbound alpha-actinin models. The initial models for alpha-actinin with and without Ca^{2+} in the bulk system were made from the PDB entry 1SJJ. The alpha-actinin was solvated in a 30 mM KCl solution. The system without Ca^{2+} consists of one alpha-actinin, 182 K^+, 128 Cl^-, and 251,756 water molecules. In the system with Ca^{2+}, four K^+ were removed and two Ca^{2+} were placed at the center of C_γ of Asp768 and Asp771. It was confirmed that Ca^{2+} ions are stably bound to Asp residues during the simulation. The histidine residues were assumed to be in the protonation state at pH = 7, since they face the bulk solution. The size of the system was 168.856 × 325.387 × 144.838 $Å^3$. AMBER ff19SB[67], TIP3P[68], the Li and Merz 12-6[69], the Li and Merz 12-6-4[70] models

536 were employed for the proteins, water molecules, monovalent ions, and divalent ions,
537 respectively. The system was equilibrated by 1 ns MD simulations with constant
538 temperature (300 K) and pressure conditions (1 bar), followed by 10 ns MD simulations
539 with constant temperature (300 K) and volume conditions. All MD simulations were
540 performed using AMBER22 (D. A. Case, H. M. Aktulga, K. Belfon, I. Y. Ben-Shalom, J.
541 T. Berryman, S. R. Brozell, D. S. Cerutti, T. E. Cheatham, I. G. A. Cisneros, V. W. D.
542 Cruzeiro, T. A. Darden, N. Forouzesh, G. Giambasụ, T. Giese, M. K. Gilson, H. Gohlke,
543 A. W. Goetz, J. Harris, S. Izadi, S. A. Izmailov, et al., AMBER22; University of California:
544 San Francisco, 2022). A Berendsen thermostat[71] was used to control the temperature, and
545 a Monte Carlo barostat with anisotropic scaling was used to control the pressure. The
546 SHAKE algorithm[72] was used to keep the bond length having H atoms constant, enabling
547 the use of a time step of 2 fs. The periodic boundary condition was imposed, and long-
548 range interactions were calculated by the particle mesh Ewald method[73] with a 10 Å cutoff
549 in real space. After the equilibration, the MD simulation was performed for 1μs with
550 constant temperature at 300 K and volume conditions using the Berendsen thermostat[71].
551 The trajectories were saved at each 1 ns to generate 1000 configuration libraries, which
552 were used to analyse principal component (PC) modes using principal component analysis
553 (PCA) to capture the bending and twisting angles, and distances between domains.
554
555 ***Principal component analysis***
556 Before the PCA, the configuration of alpha-actinin was aligned assuming that C_α atoms in
557 the center part of the rod domain (residue 485-525) have the lowest root mean square
558 fluctuation (RMSF). To compare the conformational library of AFMfit-NMA and MD
559 simulations for Ca^{2+}-bound and Ca^{2+}-unbound states, we chose to reduce the
560 dimensionality of the libraries using PCA. We normalized the number of elements in the
561 six conformational libraries of AFMfit-NMA, AFMfit-MD, and MD simulations for Ca^{2+}-
562 bound and Ca^{2+}-unbound states, ensuring each library contains 1,000 conformations. We
563 combined these libraries to obtain a total library of 6,000 conformations. These
564 conformations were then projected onto the same subspace using PCA. Then PCA was
565 performed using singular value decomposition (SVD)[74] on the mean-subtracted C_α

566 coordinates of the combined libraries. We reduced the dimension to three principal
567 components by retaining only the principal components (PCs) that have the most impact
568 on the variance, more precisely the PCs that have an explained variance ratio (i.e. the
569 normalized squared singular values) of more than 10%. To obtain a subspace on a per-atom
570 basis, the eigenvectors were normalized by the number of C_α atoms in the system.
571
572 ***Analyses of domain distances and twisting and bending angles in alpha-actinin***
573 The ABD was divided into two domains: CH1, residue 26-138; CH2, residue 139-
574 251. EF12 is residue 749-818, and EF34 is residue 819-888. The center of C_α of each
575 domain was used to compute domain distances. Since there are four centers, there are six
576 distances.
577 For the analyses of bending and twisting angles, the alpha-actinin was aligned as
578 described in PCA. The C_α atoms in residue 485-525 were placed on the xy-plane and their
579 average coordinate was set to be the origin. The rod domain was placed along the x-axis
580 (**Fig. 6A**). The position of the center of C_α atoms of CH1 and CH2 in one chain and EF12
581 and EF34 in the other chain is denoted as (x_1, y_1, z_1) (end 1), and that of the other end (end
582 2) is denoted as (x_2, y_2, z_2). x_1 is chosen so that $x_1 > 0$, so $x_2 < 0$. The bending angle for end
583 1 was calculated by $\tan^{-1}(z_1/x_1)$, and that for end 2 by $-\tan^{-1}(z_2/x_2)$. In this definition, the
584 bending angles in alpha-actinin (PDB ID: 1SJJ) were −1.4 and 8.5 degrees.
585 For the twisting angle calculation, the position of the center of Cα atoms of CH1
586 and CH2 at end 1 is denoted as (x_{1c}, y_{1c}, z_{1c}), and that of EF12 and EF34 at end 1 is denoted
587 as (x_{1e}, y_{1e}, z_{1e}). The twisting angle for end 1 was defined as the angle between a vector
588 from the center of EF12 and EF34 to the center of CH1 and CH2 in the yz-plane and y axis
589 (**Fig. 6B**): that is, $\tan^{-1}((z_{1c} - z_{1e})/(y_{1c} - y_{1e}))$. For end 2, considering the orientation, it was
590 calculated by $\tan^{-1}(-(z_{2c} - z_{2e})/(y_{2c} - y_{2e}))$. When the twisting angle became less than −100
591 degrees, 360 degrees was added to the angle, since it is a part of the fluctuation over 180
592 degrees. In this definition, the twisting angles in alpha-actinin (PDB ID: 1SJJ) were −12.8
593 and 20.5 degrees.

Data availability

All the data are included in the Supplementary Information or as source data. The conformation libraries, available in PDB format, can be accessed upon reasonable request.

Code availability

https://gricad-gitlab.univ-grenoble-alpes.fr/GruLab/AFMfit-NMA

Acknowledgments

The authors express their gratitude for the facility and financial support provided by the WPI Nano Life Science Institute (WPI NanoLSI), Kanazawa University; the instrumental assistance provided by Toshio Ando, Noriyuki Kodera, and Hiroki Konno (WPI NanoLSI). The authors also acknowledge the financial support from KAKENHI (Japan Society for the Promotion of Science) for K.X.N. (19K06581, 23K05713, 23H02452-01) and T.S. (24K01308). The MD simulations were carried out on the supercomputers at the Research Center for Computational Science in Okazaki, Japan (Project: 24-IMS-096).

This study was also partially supported by the French National Research Agency (research grant ANR-23-CE45-0024-01) and within the framework of the "Investissements d'avenir" program (ANR-15-IDEX-02) for S.G.

Author Contributions:

K.X.N. designed the research; K.X.N., T.S., R.V. and S.G. performed the research; K.X.N., T.S., R.V., H.G.N., N.T.P.L., and S.G. analyzed the data; K.X.N., T.S., R.V. and S.G. wrote the paper.

Declaration of interests:

The authors declare that they have no competing interests.

References

1. Ando, T., Fukuda, S., Ngo, K. X. & Flechsig, H. High-Speed Atomic Force

624 Microscopy for Filming Protein Molecules in Dynamic Action. *Annu. Rev.*
625 *Biophys.* **53**, 19–39 (2024).
626 2. Ando, T. *et al.* A high-speed atomic force microscope for studying biological
627 macromolecules. *Proc. Natl. Acad. Sci. U. S. A.* **98**, 12468–12472 (2001).
628 3. Shimizu, M. *et al.* An ultrafast piezoelectric Z-scanner with a resonance frequency
629 above 1.1 MHz for high-speed atomic force microscopy. *Rev. Sci. Instrum.* **93**,
630 013701 (2022).
631 4. Ando, T., Uchihashi, T. & Fukuma, T. High-speed atomic force microscopy for
632 nano-visualization of dynamic biomolecular processes. *Prog. Surf. Sci.* **83**, 337–
633 437 (2008).
634 5. Ando, T. *et al.* High-speed AFM and nano-visualization of biomolecular
635 processes. *Pflugers Arch. Eur. J. Physiol.* **456**, 211–225 (2008).
636 6. Ngo, K. X. *et al.* Allosteric regulation by cooperative conformational changes of
637 actin filaments drives mutually exclusive binding with cofilin and myosin. *Sci.*
638 *Rep.* **6**, 1–11 (2016).
639 7. Ngo, K. X., Kodera, N., Katayama, E., Ando, T. & Uyeda, T. Q. Cofilin-induced
640 unidirectional cooperative conformational changes in actin filaments revealed by
641 high-speed atomic force microscopy. *Elife* **4**, 1–22 (2015).
642 8. Ngo, Kien Xuan, Vu, H. T., Umeda, K., Trinh, M. N., Kodera, N. & Uyeda, T.
643 Deciphering the actin structure-dependent preferential cooperative binding of
644 cofilin. *Elife* **13**, 1–37 (2024).
645 9. Yoshioka, Y. *et al.* PQBP3 prevents senescence by suppressing PSME3-mediated
646 proteasomal Lamin B1 degradation. *EMBO J.* **43**, 3968–3999 (2024).
647 10. Kodera, N. *et al.* Structural and dynamics analysis of intrinsically disordered
648 proteins by high-speed atomic force microscopy. *Nat. Nanotechnol.* **16**, 181–189
649 (2021).
650 11. Fukuda, S. & Ando, T. Faster high-speed atomic force microscopy for imaging of
651 biomolecular processes. *Rev. Sci. Instrum.* **92**, (2021).
652 12. Zwier, M. C. & Chong, L. T. Reaching biological timescales with all-atom
653 molecular dynamics simulations. *Curr. Opin. Pharmacol.* **10**, 745–752 (2010).

654 13. Hollingsworth, S. A. & Dror, R. O. Molecular dynamics simulation for all. *Neuron*
655 **99**, 1–29 (2018).
656 14. Karplus, M. & McCammon, J. A. Molecular dynamics simulations of
657 biomolecules. *Nat. Struct. Biol.* **9**, 646–652 (2002).
658 15. Kovermann, M., Rogne, P. & Wolf-Watz, M. Protein dynamics and function from
659 solution state NMR spectroscopy. *Q. Rev. Biophys.* **49**, e6 (2016).
660 16. Hu, Y. *et al.* NMR-Based Methods for Protein Analysis. *Anal. Chem.* **93**, 1866–
661 1879 (2021).
662 17. Golji, J., Collins, R. & Mofrad, M. R. K. Molecular mechanics of the α-actinin rod
663 domain: Bending, torsional, and extensional behavior. *PLoS Comput. Biol.* **5**,
664 (2009).
665 18. Adcock, S. A. & McCammon, J. A. Molecular dynamics: Survey of methods for
666 simulating the activity of proteins. *Chem. Rev.* **106**, 1589–1615 (2006).
667 19. Sumino, A., Sumikama, T., Uchihashi, T. & Oiki, S. High-speed AFM reveals
668 accelerated binding of agitoxin-2 to a K+ channel by induced fit. *Sci. Adv.* **5**, 1–10
669 (2019).
670 20. Chu, J. W. & Voth, G. A. Allostery of actin filaments: Molecular dynamics
671 simulations and coarse-grained analysis. *Proc. Natl. Acad. Sci. U. S. A.* **102**,
672 13111–13116 (2005).
673 21. Li, M. & Zheng, W. All-atom molecular dynamics simulations of actin-myosin
674 interactions: A comparative study of cardiac α myosin, β myosin, and fast skeletal
675 muscle myosin. *Biochemistry* **52**, 8393–8405 (2013).
676 22. Yu, I. *et al.* Biomolecular interactions modulate macromolecular structure and
677 dynamics in atomistic model of a bacterial cytoplasm. *Elife* **5**, 1–22 (2016).
678 23. Lindorff-Larsen, K., Piana, S., Dror, R. O. & Shaw, D. E. How fast-folding
679 proteins fold. *Science (80-.).* **334**, 517–520 (2011).
680 24. Vakser, I. A., Grudinin, S., Jenkins, N. W., Kundrotas, P. J. & Deeds, E. J.
681 Docking-based long timescale simulation of cell-size protein systems at atomic
682 resolution. *Proc. Natl. Acad. Sci. U. S. A.* **119**, 1–8 (2022).
683 25. Feig, M. & Sugita, Y. Whole-cell models and simulations in molecular detail.

684 *Annu. Rev. Cell Dev. Biol.* **35**, 191–211 (2019).
685 26. Hoffmann, A. & Grudinin, S. NOLB: Nonlinear Rigid Block Normal-Mode
686 Analysis Method. *J. Chem. Theory Comput.* **13**, 2123–2134 (2017).
687 27. Tama, F. & Sanejouand, Y. H. Conformational change of proteins arising from
688 normal mode calculations. *Protein Eng.* **14**, 1–6 (2001).
689 28. Tama, F., Valle, M., Frankt, J. & Brooks, C. L. Dynamic reorganization of the
690 functionally active ribosome explored by normal mode analysis and cryo-electron
691 microscopy. *Proc. Natl. Acad. Sci. U. S. A.* **100**, 9319–9323 (2003).
692 29. Fukami, K. *et al.* Requirement of phosphatidylinositol 4,5-bisphosphate for α-
693 actinin function. *Nature* **359**, 150–152 (1992).
694 30. Fraley, T. S. *et al.* Phosphoinositide binding inhibits α-actinin bundling activity. *J.*
695 *Biol. Chem.* **278**, 24039–24045 (2003).
696 31. Taylor, K. a & Taylor, D. W. Formation of two-dimensional complexes of F-actin
697 and crosslinking proteins on lipid monolayers: demonstration of unipolar alpha-
698 actinin-F-actin crosslinking. *Biophys. J.* **67**, 1976–83 (1994).
699 32. Young, P. The interaction of titin and alpha-actinin is controlled by a
700 phospholipid-regulated intramolecular pseudoligand mechanism. *EMBO J.* **19**,
701 6331–6340 (2000).
702 33. Ribeiro, E. D. A. *et al.* The structure and regulation of human muscle α-Actinin.
703 *Cell* **159**, 1447–1460 (2014).
704 34. Liu, J., Taylor, D. W. & Taylor, K. A. A 3-D reconstruction of smooth muscle α-
705 actinin by CryoEm reveals two different conformations at the actin-binding region.
706 *J. Mol. Biol.* **338**, 115–125 (2004).
707 35. Foley, K. S. & Young, P. W. The non-muscle functions of actinins: An update.
708 *Biochem. J.* **459**, 1–13 (2014).
709 36. Pinotsis, N. *et al.* Calcium modulates the domain flexibility and function of an α-
710 actinin similar to the ancestral a-actinin. *Proc. Natl. Acad. Sci. U. S. A.* **117**,
711 22101–22112 (2020).
712 37. Tang, J., Taylor, D. W. & Taylor, K. a. The three-dimensional structure of alpha-
713 actinin obtained by cryoelectron microscopy suggests a model for Ca(2+)-

714 dependent actin binding. *J. Mol. Biol.* **310**, 845–58 (2001).
715 38. Vuillemot, R., Pellequer, J. L. & Grudinin, S. Deciphering conformational
716 dynamics in AFM data using fast nonlinear NMA and FFT-based search with
717 AFMFit. *Commun. Biol.* **8**, 1–13 (2025).
718 39. Shams, H., Golji, J., Garakani, K. & Mofrad, M. R. K. Dynamic Regulation of α-
719 Actinin's Calponin Homology Domains on F-Actin. *Biophys. J.* **110**, 1444–1455
720 (2016).
721 40. Uchihashi, T., Kodera, N. & Ando, T. Guide to video recording of structure
722 dynamics and dynamic processes of proteins by high-speed atomic force
723 microscopy. *Nat. Protoc.* **7**, 1193–1206 (2012).
724 41. Kodera, N., Yamamoto, D., Ishikawa, R. & Ando, T. Video imaging of walking
725 myosin V by high-speed atomic force microscopy. *Nature* **468**, 72–76 (2010).
726 42. Voss, J. M., Harder, O. F., Olshin, P. K., Drabbels, M. & Lorenz, U. J. Rapid
727 melting and revitrification as an approach to microsecond time-resolved cryo-
728 electron microscopy. *Chem. Phys. Lett.* **778**, 138812 (2021).
729 43. Bongiovanni, G., Harder, O. F., Drabbels, M. & Lorenz, U. J. Microsecond
730 melting and revitrification of cryo samples with a correlative light-electron
731 microscopy approach. *Front. Mol. Biosci.* **9**, 1–7 (2022).
732 44. Lorenz, U. J. Microsecond time-resolved cryo-electron microscopy. *Curr. Opin.*
733 *Struct. Biol.* **87**, 102840 (2024).
734 45. Vuillemot, R., Miyashita, O., Tama, F., Rouiller, I. & Jonic, S. NMMD: Efficient
735 Cryo-EM Flexible Fitting Based on Simultaneous Normal Mode and Molecular
736 Dynamics atomic displacements. *J. Mol. Biol.* **434**, 167483 (2022).
737 46. Boehr, D. D., Dyson, H. J. & Wright, P. E. An NMR perspective on enzyme
738 dynamics. *Chem. Rev.* **106**, 3055–3079 (2006).
739 47. Wolf-Watz, M. *et al.* Linkage between dynamics and catalysis in a thermophilic-
740 mesophilic enzyme pair. *Nat. Struct. Mol. Biol.* **11**, 945–949 (2004).
741 48. Purslow, J. A., Khatiwada, B., Bayro, M. J. & Venditti, V. NMR Methods for
742 Structural Characterization of Protein-Protein Complexes. *Front. Mol. Biosci.* **7**,
743 1–8 (2020).

744 49. Camacho-Zarco, A. R. *et al.* NMR Provides Unique Insight into the Functional
745 Dynamics and Interactions of Intrinsically Disordered Proteins. *Chem. Rev.* **122**,
746 9331–9356 (2022).
747 50. Moraes, A. H. & Valente, A. P. Conformational dynamics and kinetics of protein
748 interactions by nuclear magnetic resonance. *J. Magn. Reson. Open* **14–15**, 100093
749 (2023).
750 51. Murata, K. & Wolf, M. Cryo-electron microscopy for structural analysis of
751 dynamic biological macromolecules. *Biochim. Biophys. Acta - Gen. Subj.* **1862**,
752 324–334 (2018).
753 52. Gauto, D. F. *et al.* Integrated NMR and cryo-EM atomic-resolution structure
754 determination of a half-megadalton enzyme complex. *Nat. Commun.* **10**, 1–12
755 (2019).
756 53. Schanda, P. & Haran, G. NMR and Single-Molecule FRET Insights into Fast
757 Protein Motions and Their Relation to Function. *Annu. Rev. Biophys.* **53**, 247–273
758 (2024).
759 54. Lorenz, M., Popp, D. & Holmes, K. C. Refinement of the F-actin model against x-
760 ray fiber diffraction data by the use of a directed mutation algorithm. *J. Mol. Biol.*
761 **234**, 826–836 (1993).
762 55. Oda, T., Iwasa, M., Aihara, T., Maéda, Y. & Narita, A. The nature of the globular-
763 to fibrous-actin transition. *Nature* **457**, 441–445 (2009).
764 56. Fujii, T., Iwane, A. H., Yanagida, T. & Namba, K. Direct visualization of
765 secondary structures of F-actin by electron cryomicroscopy. *Nature* **467**, 724–728
766 (2010).
767 57. Murakami, K. *et al.* Structural basis for actin assembly, activation of ATP
768 hydrolysis, and delayed phosphate release. *Cell* **143**, 275–287 (2010).
769 58. González, M. A. Force fields and molecular dynamics simulations. *Collect. SFN*
770 **12**, 169–200 (2011).
771 59. Chmiela, S., Sauceda, H. E., Müller, K. R. & Tkatchenko, A. Towards exact
772 molecular dynamics simulations with machine-learned force fields. *Nat. Commun.*
773 **9**, 1–10 (2018).

60. Bhavna, R. & Sonawane, M. A deep learning framework for quantitative analysis of actin microridges. *npj Syst. Biol. Appl.* **9**, 1–15 (2023).
61. Degenhardt, M. F. S. *et al.* Determining structures of RNA conformers using AFM and deep neural networks. *Nature* **637**, (2025).
62. Vinh, T., Nguyen, T., Ly, N. Q., Thi, N. & Le, P. AFMnanoSALQ: An Accurate Detection Framework for Semi-Automatic Labeling and Quantitative Analysis of α-Hemolysin Nanopores Using Intensity-Height Cues in HS-AFM Data. *bioRxiv* (2025). doi:10.1101/2025.02.26.640237
63. Jiang, Y., Wang, Z. & Scheuring, S. A structural biology compatible file format for atomic force microscopy. *Nat. Commun.* **16**, 1–16 (2025).
64. Sumikama, T. *et al.* Computed Three-Dimensional Atomic Force Microscopy Images of Biopolymers Using the Jarzynski Equality. *J. Phys. Chem. Lett.* **13**, 5365–5371 (2022).
65. Ngo, K. X. *et al.* Allosteric regulation by cooperative conformational changes of actin filaments drives mutually exclusive binding with cofilin and myosin. *Sci. Rep.* **6**, 1–11 (2016).
66. Pu Liu, Dimitris K. Agrafiotis, D. L. T. Rapid Communication Fast Determination of the Optimal Rotational Matrix for Macromolecular Superpositions. *J. Comput. Chem.* **31**, 1561–1563 (2010).
67. Tian, C. *et al.* Ff19SB: Amino-Acid-Specific Protein Backbone Parameters Trained against Quantum Mechanics Energy Surfaces in Solution. *J. Chem. Theory Comput.* **16**, 528–552 (2020).
68. William L. Jorgensen, Jayaraman Chandrasekhar, and J. D. M. Comparison of simple potential functions for simulating liquid water. *J. Chem. Phys.* **79**, 926–935 (1983).
69. Li, P., Song, L. F. & Merz, K. M. Systematic parameterization of monovalent ions employing the nonbonded model. *J. Chem. Theory Comput.* **11**, 1645–1657 (2015).
70. Li, P. & Merz, K. M. Taking into account the ion-induced dipole interaction in the nonbonded model of ions. *J. Chem. Theory Comput.* **10**, 289–297 (2014).

71. Berendsen, H. J. C., Postma, J. P. M., Van Gunsteren, W. F., Dinola, A. & Haak, J. R. Molecular dynamics with coupling to an external bath. *J. Chem. Phys.* **81**, 3684–3690 (1984).

72. Ryckaert, J. P., Ciccotti, G. & Berendsen, H. J. C. Numerical integration of the cartesian equations of motion of a system with constraints: molecular dynamics of n-alkanes. *J. Comput. Phys.* **23**, 327–341 (1977).

73. Essmann, U. *et al.* A smooth particle mesh Ewald method. *J. Chem. Phys.* **103**, 8577–8593 (1995).

74. Wall, M. E., Rechtsteiner, A. & Rocha, L. M. Singular Value Decomposition and Principal Component Analysis. in *A Practical Approach to Microarray Data Analysis* 91–109 (2005). doi:10.1007/0-306-47815-3_5

75. Amyot, R. & Flechsig, H. BioAFMviewer: An interactive interface for simulated AFM scanning of biomolecular structures and dynamics. *PLoS Comput. Biol.* **16**, 1–12 (2020).

Graphic Abstract

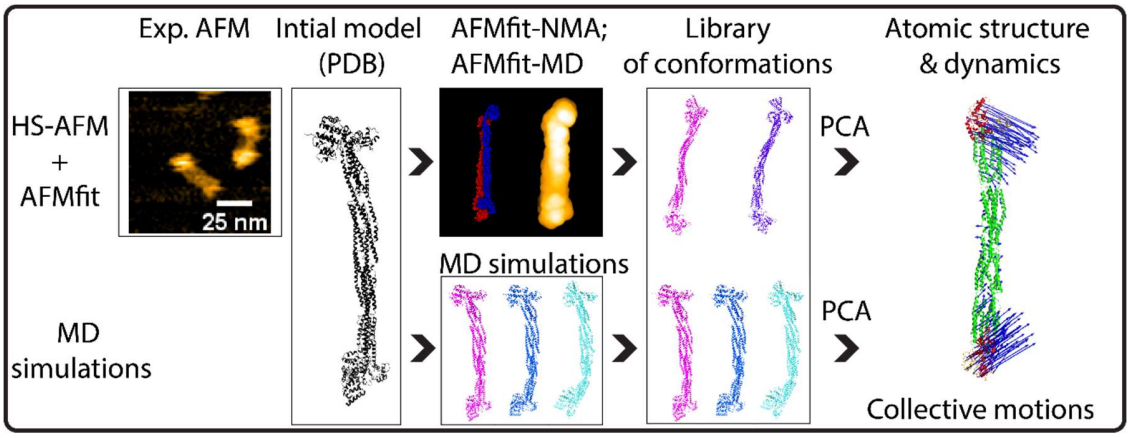

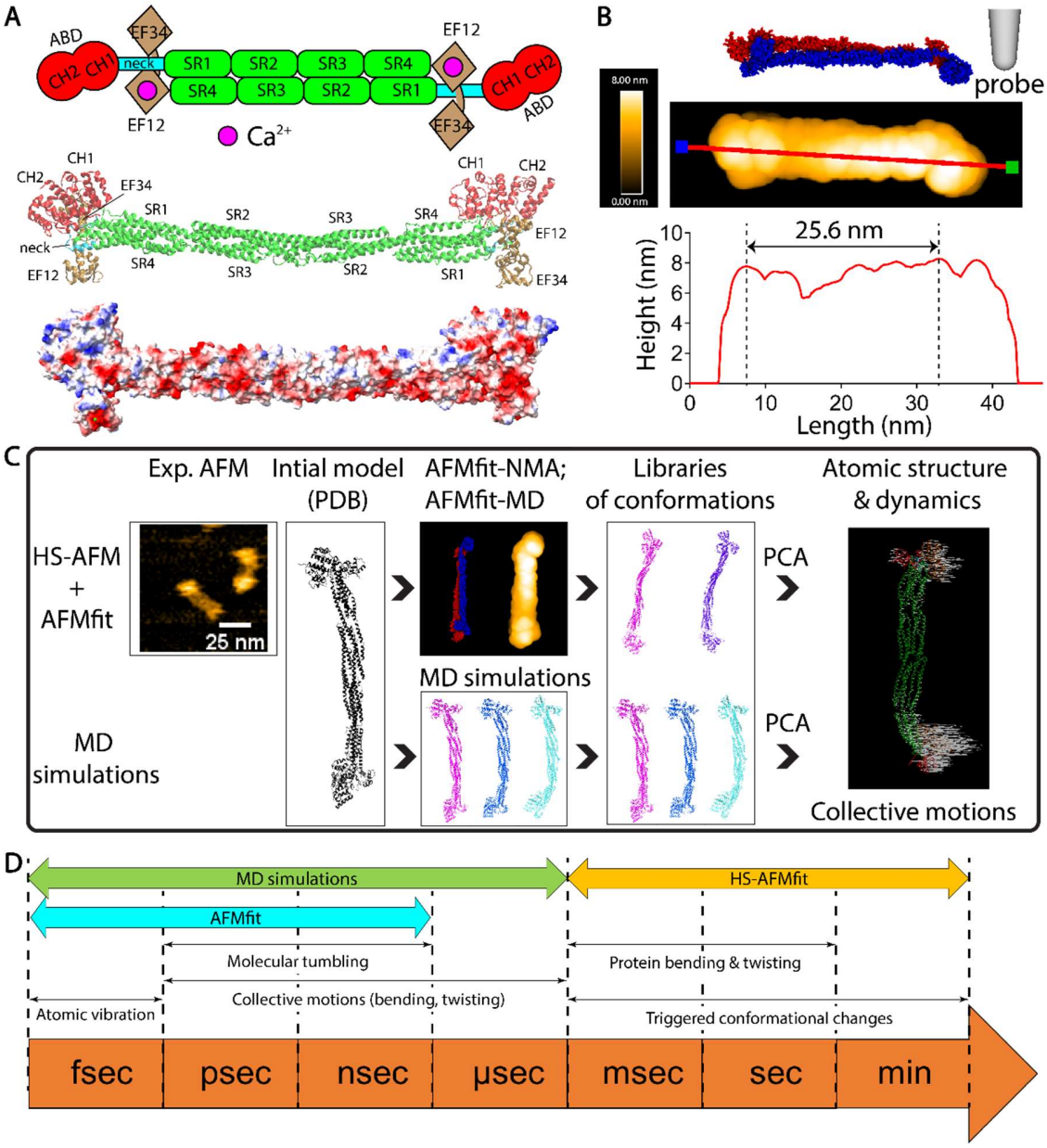

Fig. 1 Novel workflow for analyzing the dynamics and atomic structures of alpha-actinin through the integration of HS-AFM with the AFMfit-NMA, AFMfit-MD, and MD simulations.

845 (**A**) Domain composition and structure of chicken gizzard smooth muscle alpha-actinin
846 (PDB: 1SJJ) depicted in a ribbon model and an electrostatic surface potential model. In the
847 latter, red and blue represent negative and positive charges, respectively. Alpha-actinin is
848 an antiparallel homodimer with a molecular weight exceeding 200 kDa. It comprises an N-
849 terminal actin binding domain (ABD), in which the two calponin homology 1 and 2 (CH1,
850 CH2) domains are in extensive contact, a central region containing four spectrin-like repeat
851 (SR1-SR4) or rod domains, and a C-terminal calmodulin-like domain (CaMD) that
852 includes two pairs of EF-hand motifs (EF12 and EF34). The EF12 domain is responsible
853 for the Ca^{2+} binding. The two ABDs undergo a 90-degree rotation, enabling alpha-actinin
854 to crosslink the actin filaments in nearly any orientation.
855 (**B**) Pseudo-AFM images and topographic cross-sectional profile of alpha-actinin
856 generated with the AFM viewer[75]. The pseudo-AFM images were obtained with the
857 following scan parameters: step size, 0.1 nm; cone angle, 5°; and tip radius, 2.0 nm. The
858 cross-sectional profile in the bottom panel corresponds to the red line in the middle panel.
859 (**C**) Workflow for developing libraries of conformations, storing them as PDB files, and
860 analyzing the dynamics and atomic structures of alpha-actinin through the integration of
861 HS-AFM with the AFMfit-NMA or AFMfit-MD, and molecular dynamics (MD)
862 simulations. This process is followed by principal component analysis (PCA) to identify
863 and classify dynamic atomic structures into distinct modes of collective motion (indicated
864 by white arrows).
865 (**D**) Protein atomic conformational dynamics over timescales resolved by MD simulations
866 and HS-AFM. Typically, protein conformational dynamics were resolved over
867 nanosecond–second timescales using AFMfit, all-atom MD simulations, and HS-AFM.
868
869
870
871
872
873
874

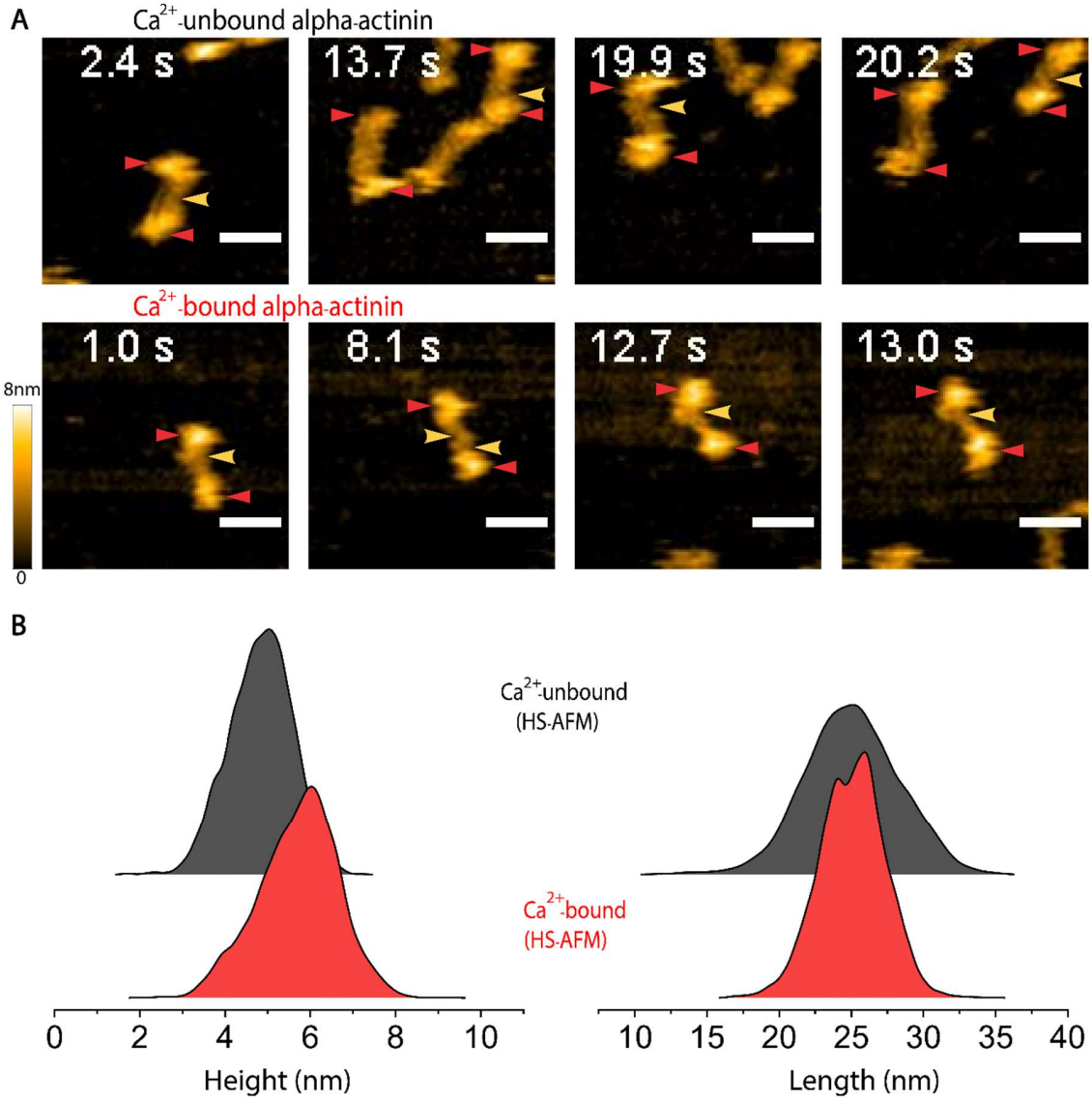

Fig. 2 HS-AFM visualizes the 3D surface structure and millisecond conformational dynamics of alpha-actinin.

(**A**) HS-AFM still images showing the various physical motions of alpha-actinin, such as twisting and bending, with and without Ca^{2+} binding. Yellow and red arrowheads denote bending and twisting motions, respectively, in the rod and neck domains. Scale bars: 25 nm. Color scale: 0–8 nm.

882 (**B**) Ridgeline plots displaying the distribution of the peak heights and lengths between the
883 two ABDs for Ca^{2+}-bound (5.7 ± 0.9 nm, 25.1 ± 2.3 nm) and Ca^{2+}-unbound (4.8 ± 0.7 nm,
884 25.0 ± 3.2 nm) alpha-actinin obtained with HS-AFM. A two-sample t-test ($p \leq 0.05$)
885 indicates that the difference in height distributions between the bound and unbound states
886 is significant ($p = 0$), whereas the difference in length distributions is not significant ($p =$
887 0.78736). Related to **Supplementary Table 1**.
888
889
890
891
892
893
894
895
896
897
898
899
900
901
902
903
904
905
906
907
908
909
910
911

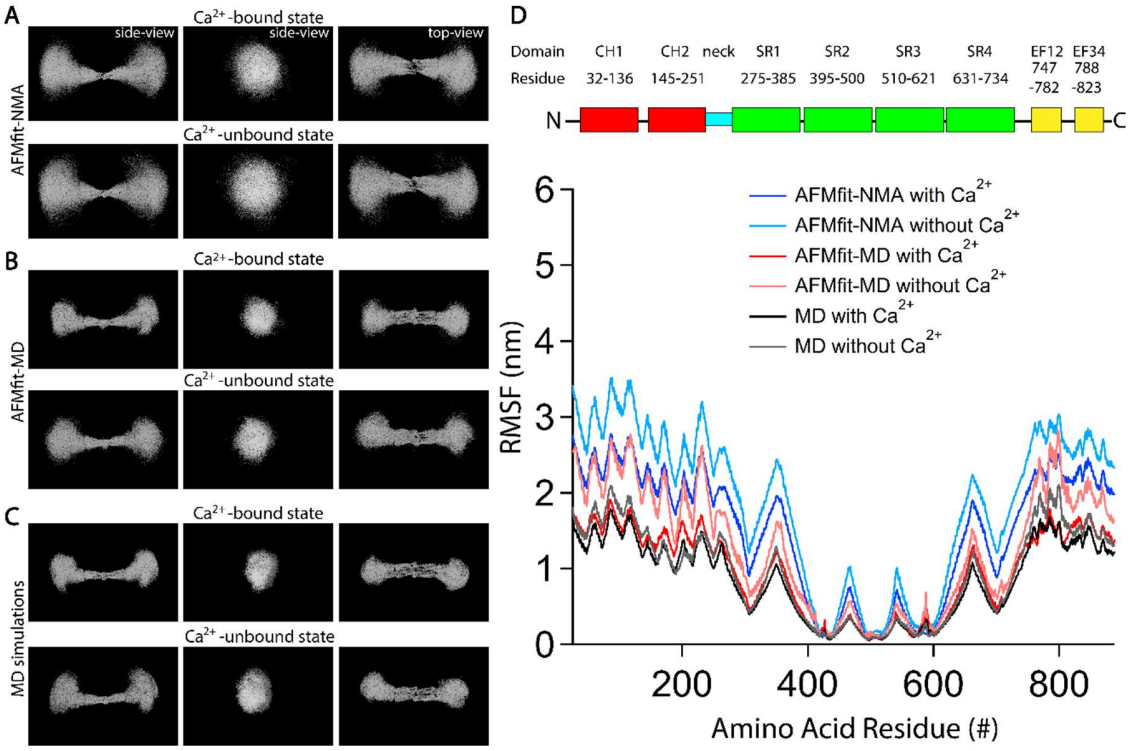

Fig. 3 Analyses of the dynamics and atomic structure of the Ca^{2+}-bound and unbound alpha-actinin using AFMfit-NMA, AFMfit-MD, and MD simulations.

(**A, B, C**) Positions of the Cα atoms from the libraries of the Ca^{2+}-bound and Ca^{2+}-unbound alpha-actinin conformations obtained from the AFMfit-NMA, AFMfit-MD, and MD simulations, respectively. The conformations were aligned, assuming that the helical elements in the SR2 and SR3 domains (residues 485-525) exhibited the lowest root mean square fluctuation (RMSF). Top views and two different side views are presented to compare the molecular dynamics among the states and conformation libraries.

(**D**) Root mean square fluctuation (RMSF) values plotted against the residue number. The illustration of the alpha-actinin domains, along with their corresponding amino acid residues, is based on PDB ID 1SJJ, using colors consistent with those in **Fig. 1A**. From the N-terminus to the C-terminus: CH1, CH2: calponin homology 1 and 2; SR1-SR4: spectrin-like repeat 1-4; and EF12, EF34: EF hand motifs 12, 34.

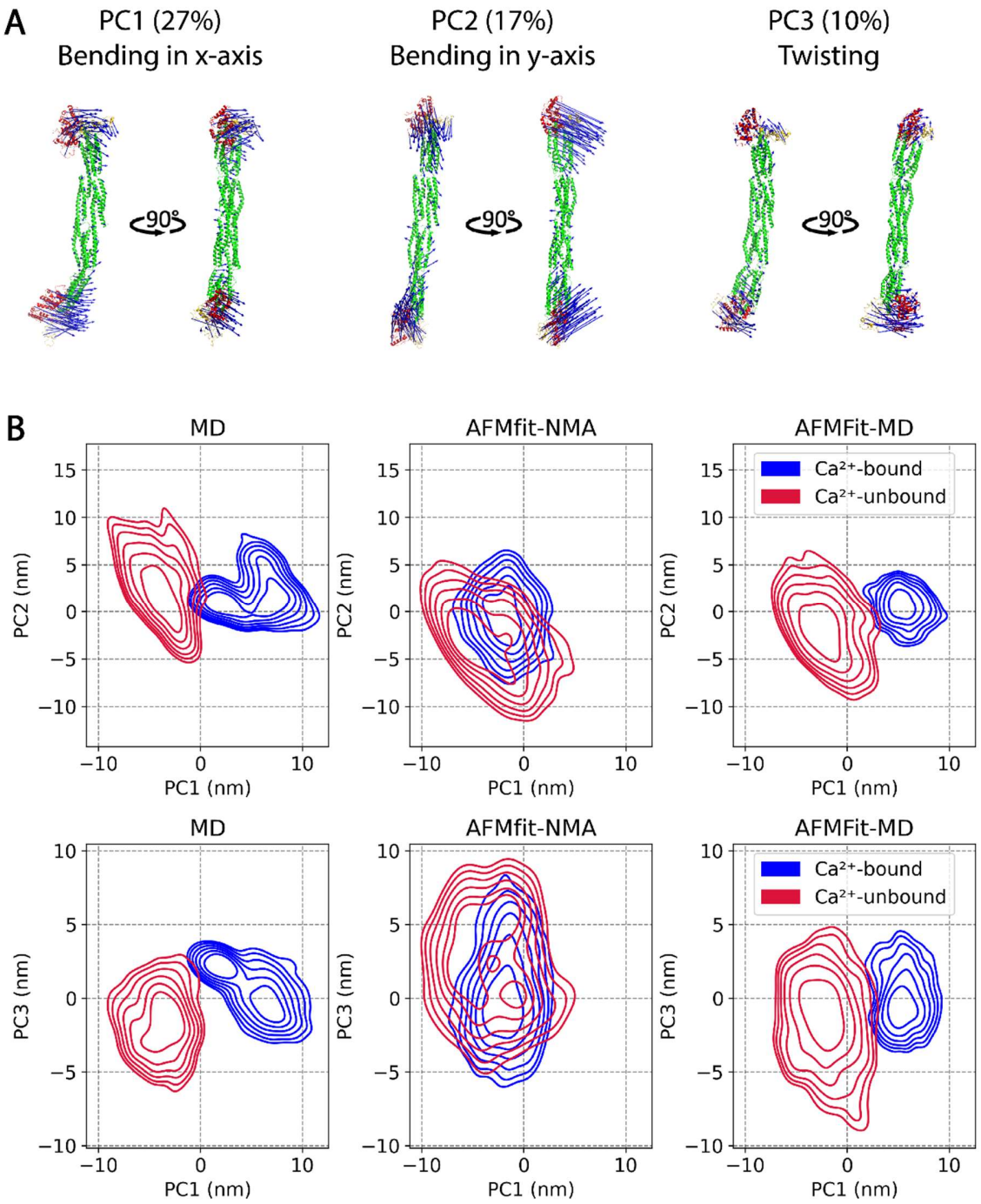

929

930 **Fig. 4 Analyses of the dynamics and atomic structure of the Ca^{2+}-bound and Ca^{2+}-**
931 **unbound alpha-actinin using HS-AFM combined with the AFMfit-NMA or AFMfit-**
932 **MD, and MD simulations.**

933 (A) Ensemble motions of the atomic conformations of alpha-actinin projected onto a
934 common PCA space according to the conformational libraries of Ca^{2+}-bound and Ca^{2+}-
935 unbound alpha-actinin obtained from the AFMfit-NMA, AFMfit-MD, and MD simulations.
936 The eigenvalues of the principal components (PC1, PC2, PC3) were used to calculate the
937 contributions (in percentages) of each motion to the total motions of alpha-actinin in the
938 two states. The alpha-actinin structures are illustrated in the tube conformations, with the
939 ABD, neck, rod, and EF12-EF34 domains represented in red, cyan, green, and yellow,
940 respectively; the eigenvector components indicating the direction of motion are shown with
941 blue arrows.
942 (B) Distributions of PC1, PC2, and PC3 values. Data obtained from conformational
943 libraries generated by AFMfit-NMA, AFMfit-MD, and MD simulations are shown in blue
944 for the Ca^{2+}-bound and in red for the Ca^{2+}-unbound states of alpha-actinin.
945 .
946
947
948
949
950
951
952
953
954
955
956
957
958
959
960
961
962

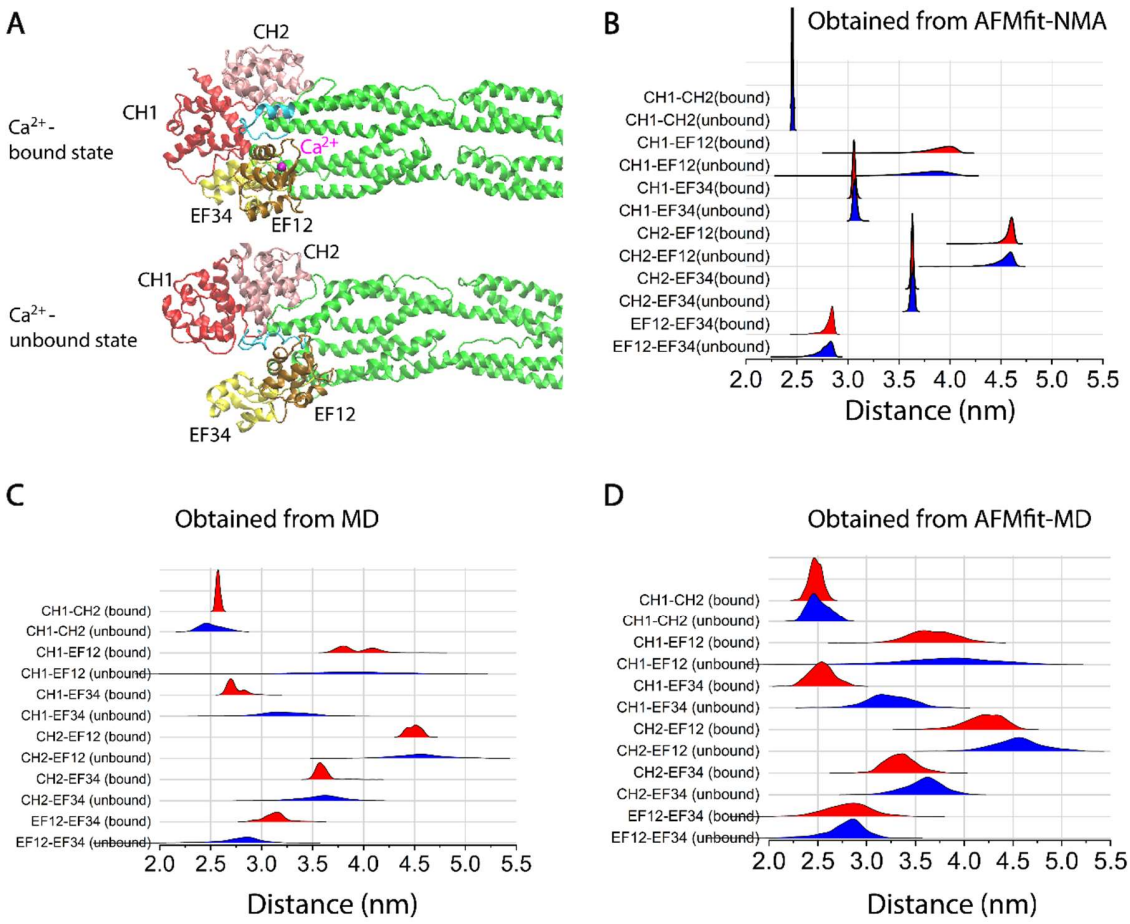

Fig. 5 Analysis of domain distances in Ca^{2+}-bound and Ca^{2+}-unbound alpha-actinin based on conformations obtained from AFMfit-NMA, AFMfit-MD, and MD simulations.

(**A**) Structural comparison of Ca^{2+}-bound and Ca^{2+}-unbound alpha-actinin, showing the positions of the CH1, CH2, EF12, and EF34 domains.

(**B, C, D**) Distribution of distances between the CH1, CH2, EF12, and EF34 domains in Ca^{2+}-bound (N = 1466) and Ca^{2+}-unbound (N = 1140) alpha-actinin derived from AFMfit-NMA, AFMfit-MD (N = 1000), and MD (N = 1000) conformations, respectively. The domain distances were measured separately for chain 1 and chain 2 in individual conformations (stored as PDB files) for both Ca^{2+}-bound and Ca^{2+}-unbound states. The final data represent the averaged values of the two chains. Related to **Supplementary Table 2**.

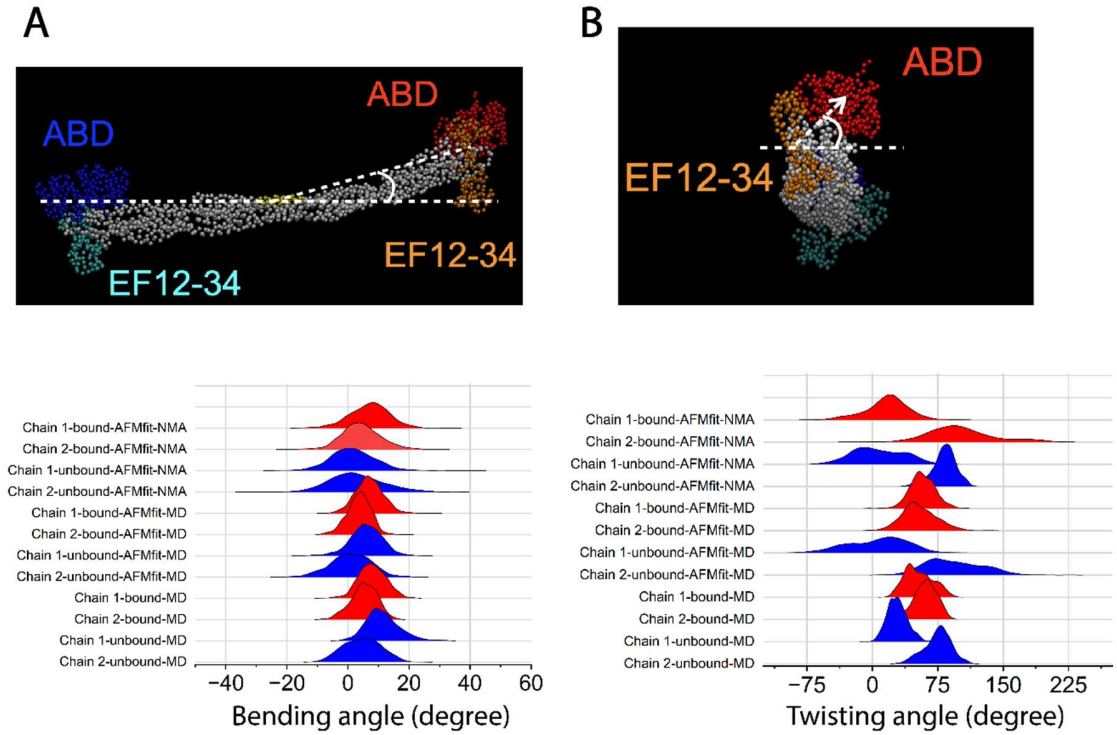

Fig. 6 Analysis of the bending (A) and twisting (B) angles of the ABD relative to the rod domain of Ca^{2+}-bound and Ca^{2+}-unbound alpha-actinin using the conformations obtained from AFMfit-NMA, AFMfit-MD, and MD simulations. Related to **Supplementary Table 3.**

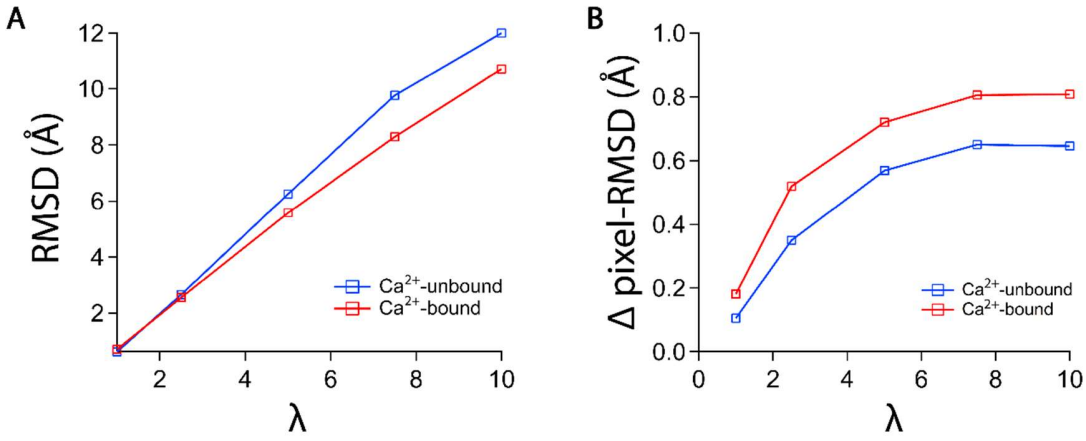

Supplementary Figure 1 Optimization of the flexible fitting parameter (λ)
The flexible fitting balanced structural preservation and data similarity, controlled by λ. An exhaustive search on sample particles identified the optimal λ = 7.5, yielding an average RMSD of ~10 Å from the initial model, consistent with conformational motions observed in MD simulations of α-actinin.

Supplementary Video 1 HS-AFM imaging of structure and dynamic conformational changes of Ca^{2+}-bound and Ca^{2+}-unbound alpha-actinin in solution. The AFM images were smoothed with a Gaussian filter (σ = 1). Imaging rate was done at 100 ms per frame. The Supplementary Video plays at 5 fps. Scale bars: 25 nm.

Supplementary Video 2 The HS-AFM Supplementary Videos of Ca^{2+}-bound alpha-actinin (left) and the atomic model (right) that were obtained through rigid and flexible fitting using AFMfit-NMA.

Supplementary Video 3 The HS-AFM Supplementary Videos of Ca^{2+}-unbound alpha-actinin (left) and the atomic model (right) that were obtained through rigid and flexible fitting using AFMfit-NMA.

Supplementary Video 4 PC1 captured the ensemble of bending motions in the x-axis of alpha-actinin.

1017 **Supplementary Video 5** PC2 captured the ensemble of bending motions in the y-axis of
1018 alpha-actinin.
1019
1020 **Supplementary Video 6** PC3 captured the ensemble of twisting motions of alpha-actinin.
1021
1022 **Supplementary Table 1** Summary of the height and length (mean ± SD) distributions of
1023 ABDs in Ca^{2+}-bound and Ca^{2+}-unbound alpha-actinin analyzed using conformations
1024 obtained from HS-AFM. Statistical differences were assessed using a two-population *t-*
1025 *test*, with a significant difference confirmed at $p \leq 0.05$. Related to **Figure 2.**

	Height (nm) (N)	Length (nm) (N)
Ca^{2+}-bound state	5.7 ± 0.9 (6080)	25.1 ± 2.3 (3040)
Ca^{2+}-unbound state	4.8 ± 0.7 (3885)	25.0 ± 3.2 (1941)
p-value (*t-test*)	0	0.78736

1026
1027
1028 **Supplementary Table 2** Summary of the distances between domains (mean ± SD) in
1029 Ca^{2+}-bound and Ca^{2+}-unbound alpha-actinin, derived from conformational libraries
1030 obtained from AFMfit-NMA, AFMfit-MD, and MD simulations. The domain distances
1031 were measured separately for chain 1 and chain 2 in individual conformations (stored as
1032 PDB files) for both Ca^{2+}-bound and Ca^{2+}-unbound states. The final data represent the
1033 averaged values of the two chains. A two-population *t-test* was conducted to evaluate the
1034 statistical difference ($p \leq 0.05$) between the mean values of the Ca^{2+}-bound and Ca^{2+}-
1035 unbound states. **Related to Figure 5.**

Domain distance (nm)	Ca^{2+}-bound/ AFMfit-NMA	Ca^{2+}-unbound/ AFMfit-NMA	*t-test* (*p*-value)
CH1-CH2	2.45 ± 0.01	2.46 ± 0.01	4.6×10^{-10}
CH1-EF12	3.89 ± 0.16	3.76 ± 0.21	1.9×10^{-62}
CH1-EF34	3.06 ± 0.01	3.07 ± 0.02	8.7×10^{-38}
CH2-EF12	4.58 ± 0.06	4.53 ± 0.09	1.8×10^{-49}
CH2-EF34	3.63 ± 0.01	3.63 ± 0.02	1.5×10^{-08}
EF12-EF34	2.81 ± 0.05	2.78 ± 0.07	7.7×10^{-48}
N	1466	1140	

Domain distance (nm)	Ca^{2+}-bound/ AFMfit-MD	Ca^{2+}-unbound/ AFMfit-MD	*t-test* (*p*-value)
CH1-CH2	2.48 ± 0.07	2.51 ± 0.11	$6.8x10^{-14}$
CH1-EF12	3.68 ± 0.23	3.80 ± 0.51	$4.0x10^{-12}$
CH1-EF34	2.54 ± 0.13	3.23 ± 0.23	0
CH2-EF12	4.20 ± 0.20	4.54 ± 0.26	$2.1x10^{-191}$
CH2-EF34	3.35 ± 0.16	3.58 ± 0.20	$2.9x10^{-152}$
EF12-EF34	2.81 ± 0.24	2.78 ± 0.21	$2.7x10^{-3}$
N	1000	1000	

Domain distance (nm)	Ca^{2+}-bound/ MD	Ca^{2+}-unbound/ MD	*t-test* (*p*-value)
CH1-CH2	2.57 ± 0.02	2.51 ± 0.11	$1.5x10^{-69}$
CH1-EF12	3.94 ± 0.19	3.80 ± 0.51	$2.5x10^{-17}$

CH1-EF34	2.74 ± 0.09	3.23 ± 0.23	0
CH2-EF12	4.49 ± 0.07	4.54 ± 0.26	5.3×10^{-9}
CH2-EF34	3.59 ± 0.08	3.58 ± 0.20	0.06059
EF12-EF34	3.14 ± 0.12	2.78 ± 0.21	0
N	1000	1000	

Supplementary Table 3 Summary of the bending and twisting angles of the ABD (mean ± SD) near the neck domain relative to the rod domain in Ca^{2+}-bound and Ca^{2+}-unbound alpha-actinin, derived from conformational libraries obtained from AFMfit and MD simulations. A two-population *t-test* was conducted to evaluate the statistical difference ($p \leq 0.05$) between the mean values of the Ca^{2+}-bound and Ca^{2+}-unbound states obtained from AFMfit or MD simulations. **Related to Figure 6**.

Figure 6A	Bending angle (degree)	N
Chain 1-Ca^{2+}-bound-AFMfit-NMA	7.0 ± 6.7	1466
Chain 2-Ca^{2+}-bound-AFMfit-NMA	4.3 ± 6.5	1466
Chain 1-Ca^{2+}-unbound-AFMfit-NMA	1.7 ± 7.7	1140
Chain 2-Ca^{2+}-unbound-AFMfit-NMA	2.8 ± 8.9	1140
Chain 1-Ca^{2+}-bound-AFMfit-MD	7.0 ± 4.5	1000
Chain 2-Ca^{2+}-bound-AFMfit-MD	3.6 ± 3.9	1000
Chain 1-Ca^{2+}-unbound-AFMfit-MD	6.0 ± 5.3	1000
Chain 2-Ca^{2+}-unbound-AFMfit-MD	1.0 ± 6.7	1000
Chain 1-Ca^{2+}-bound-MD	8.0 ± 4.5	1000
Chain 2-Ca^{2+}-bound-MD	5.3 ± 4.3	1000
Chain 1-Ca^{2+}-unbound-MD	11.3 ± 5.5	1000
Chain 2-Ca^{2+}-unbound-MD	4.7 ± 6.1	1000
Figure 6B	Twisting angle (degree)	N
Chain 1-Ca^{2+}-bound-AFMfit-NMA	16.7 ± 24.6	1466
Chain 2-Ca^{2+}-bound-AFMfit-NMA	101.2 ± 37.5	1466
Chain 1-Ca^{2+}-unbound-AFMfit-NMA	7.5 ± 29.4	1140
Chain 2-Ca^{2+}-unbound-AFMfit-NMA	128.6 ± 41.5	1140
Chain 1-Ca^{2+}-bound-AFMfit-MD	57.7 ± 14.5	1000
Chain 2-Ca^{2+}-bound-AFMfit-MD	53.7 ± 19.8	1000

Chain 1-Ca^{2+}-unbound-AFMfit-MD	6.3 ± 33.2	1000
Chain 2-Ca^{2+}-unbound-AFMfit-MD	93.6 ± 32.1	1000
Chain 1-Ca^{2+}-bound-MD	53.4 ± 16.2	1000
Chain 2-Ca^{2+}-bound-MD	61.5 ± 12.5	1000
Chain 1-Ca^{2+}-unbound-MD	28.5 ± 11.4	1000
Chain 2-Ca^{2+}-unbound-MD	74.9 ± 15.3	1000

1044